ELSEVIER

Earth and Planetary Science Letters 189 (2001) 253–267

EPSL

www.elsevier.com/locate/epsl

A kinematic model for recrystallization and texture development in olivine polycrystals

É. Kaminski *, N.M. Ribe

Laboratoire de Dynamique des Systèmes Géologiques, IPG Paris, 4 Place Jussieu, 75252 Paris Cedex 05, France

Received 16 January 2001; accepted 23 April 2001

Abstract

The interpretation of seismic anisotropy in the mantle requires a knowledge of the relationship between the lattice preferred orientation (LPO) of crystals and the convective flow field. In order better to understand this link, we present a model for the evolution of LPO in olivine aggregates that deform by both intracrystalline slip and dynamic recrystallization. Dynamic recrystallization depends on the dislocation density of the grains, which is a function of the applied local stress. Grains with a large density of dislocations lower their bulk strain energy by nucleating strain-free sub-grains at a rate proportional to a dimensionless nucleation parameter λ^*. Grains with high energy are then invaded by grains with low energy by grain-boundary migration, at a rate proportional to a dimensionless grain-boundary mobility M^*. The value of λ^* is constrained by observed LPO patterns in experimentally deformed olivine aggregates, and M^* is constrained by the temporal evolution of the strength of the LPO. For $M^* = 125 \pm 75$ and $\lambda^* > 3$, the model predictions agree well with the experimental results. Numerical calculations of LPO using our model are significantly faster than those based on viscoplastic self-consistent or equilibrium-based theories, making the model especially suitable for applications for complex convective flows.

Keywords: dynamic metamorphism; recrystallization; seismic city; anisotropy

1. Introduction

Much of the upper mantle (above 400 km) is known to be anisotropic [1]. Its anisotropy is both radial and azimuthal [2], and is manifested by shear wave splitting [3], by the discrepancy between Rayleigh and Love wave dispersion, and by the azimuthal dependence of body wave velocity [4,5]. One way to produce such an anisotropy is lattice preferred orientation (LPO) of anisotropic crystals in an aggregate [6]. Olivine ($(Mg_{0.9}Fe_{0.1}O)_2SiO_4$) is the major mineralogical component of the upper mantle and is characterized by a velocity difference between its fast and slow axis of 25% for V_P and 22% for V_S [7]. The observed mantle anisotropy can thus arise from the preferred orientation of olivine crystals in the convective flow [8]. A model for the evolution of LPO in olivine is then necessary to interpret seismic anisotropy in the mantle.

The relationship between plastic deformation of

* Corresponding author. E-mail: kaminski@ipgp.jussieu.fr
E-mail: ribe@ipgp.jussieu.fr

0012-821X/01/$ – see front matter
PII: S0012-821X(01)00356-9

olivine and LPO has been studied using a variety of models, including viscoplastic self-consistent (VPSC) [9], kinematic constraint [10] and stress equilibrium models [11]. A critical review of these models is given by [12]. In these models, crystals deform solely by slip on a small number (usually three) independent slip systems, and the effects of recrystallization are neglected. Under such conditions, the models predict that the LPO of an initially isotropic aggregate is such that the *a*-axis of olivine is aligned with the longest semi-axis of the finite strain ellipsoid (FSE) [9,12,13]. Such predictions are in agreement with experimental results for small (shear strain $< 50\%$) deformations of olivine in simple shear [14].

However, experiments on olivine aggregates deformed in simple shear [14] show that at large strain and high temperatures, the LPO no longer follows the FSE; instead, the dominant slip plane (010) and slip direction [100] coincide with the shear plane and the shear direction, respectively. Such an evolution is associated with intensive dynamic recrystallization, by sub-grain rotation and grain-boundary migration (GBM). Convection in the Earth induces large finite strains and hence dynamic recrystallization is likely to control the LPO and the related anisotropy. If one wants to interpret the anisotropy observations in terms of mantle flow, one thus needs a theoretical model for the relationship between deformation, dynamic recrystallization and the resulting LPO.

Since the early work of Etchecopar [15] many models have been developed to account for dynamic recrystallization. The first generation of successful models (e.g. [16]) were based on the assumption that certain orientations (hard or soft ones) were favored during recrystallization. However, there was no 'natural' physical justification for the selection of the favored orientations. Recently, a big step towards a more realistic model has been made by Wenk and coworkers for quartz and calcite [17] and for olivine [18]. In their model, the selection of the favored orientations is made via probabilistic nucleation and growth processes. They first calculate the deformation of the crystals in the aggregate using the VPSC theory. From the deformation of each crystal, they estimate a strain hardening, and thence the stored strain energy of the grains. Grains with a high strain energy are invaded by grains with low strain energy, by GBM. However, grains with a large-strain energy have also a larger nucleation probability and are likely to nucleate new grains with a low density of dislocations, which will thus grow preferentially. The LPO predicted by this model is a function of the coefficient of strain hardening, the relation between strain hardening and strain energy, the grain-boundary mobility, and three additional parameters describing the nucleation process. For suitably chosen values of the free parameters, the predictions of the model are in good agreement with the large-strain experimental results of Zhang and Karato [14].

However, the model of Wenk and coworkers [17,18] has some limitations which motivate the present work. The model contains a large number (six) of free parameters for which few experimental constraints are available, making extrapolation to the Earth's mantle difficult. Further, the predicted LPO was compared with only a single 'snapshot' of the texture developed in simple shear; its evolution as a function of strain and of deformation type was not investigated. Finally, the VPSC approach is computationally expensive, and becomes unstable for large deformations when the LPO is strong. A VPSC-based model is therefore impractical for incorporation into numerical convection codes.

Here we present a simpler theory for dynamic recrystallization of olivine aggregates, based on a kinematic constraint model for plastic deformation [10]. The model treats dynamic recrystallization by estimating the dislocation density in the crystals as a function of their orientation, and involves only two free parameters, a dimensionless grain-boundary mobility and a dimensionless nucleation coefficient. We constrain the values of these parameters using a variety of observations, including textural 'snapshots' from experiments in simple shear [14,19] and uniaxial compression [20] and measurements of the mean orientation and variance of the LPO as functions of strain in simple shear [14]. The model affords a savings in computer time of a factor of at least 100 relative to the VPSC model, making it highly practical for geophysical applications.

$$a_{ij}^{\nu} = \begin{pmatrix} \cos\phi_2^{\nu}\cos\phi_1^{\nu} - \cos\theta^{\nu}\sin\phi_1^{\nu}\sin\phi_2^{\nu} & \cos\theta^{\nu}\cos\phi_1^{\nu}\sin\phi_2^{\nu} + \cos\phi_2^{\nu}\sin\phi_1^{\nu} & \sin\phi_2^{\nu}\sin\theta^{\nu} \\ -\sin\phi_2^{\nu}\cos\phi_1^{\nu} - \cos\theta_1^{\nu}\sin\phi_1^{\nu}\cos\phi_2^{\nu} & \cos\theta^{\nu}\cos\phi_1^{\nu}\cos\phi_2^{\nu} - \sin\phi_2^{\nu}\sin\phi_1^{\nu} & \cos\phi_2^{\nu}\sin\theta^{\nu} \\ \sin\theta^{\nu}\sin\phi_1^{\nu} & -\sin\theta^{\nu}\cos\phi_1^{\nu} & \cos\theta^{\nu} \end{pmatrix} \quad (1)$$

2. Plastic deformation

The starting point for the model of plastic deformation is the theory developed by Ribe and Yu [10]. We consider an aggregate of N crystals of volume fraction f_ν, ($\nu = 1, 2, ..., N$). The orientation of each grain relative to an external or 'laboratory' frame is described by a set of three Eulerian angles $g_\nu = (\phi_1{}^\nu,\ \theta^\nu,\ \phi_2^\nu)$ and the related matrix of direction cosines, a_{ij}^ν: *(see above)*

The quantity a_{ij}^ν is the cosine of the angle between the ith crystal axis ($i = 1, 2, 3$ for the axes [100], [010], and [001], respectively) and the ith external axis. The grains deform by intracrystalline slip, which controls the rotation of the crystallographic axes, and undergo dynamic recrystallization, which controls the evolution of the volume fractions.

The aggregate is subjected to an externally imposed macroscopic deformation described by a velocity gradient tensor:

$$L_{ij} = E_{ij} - \varepsilon_{ijk}\Omega_k \quad (2)$$

where E_{ij} is the strain rate tensor, $2\Omega_k$ is the vorticity vector, and ε_{ijk} is the alternating tensor ($\varepsilon_{ijk} = 1$ if ijk are in ascending order, $\varepsilon_{ijk} = -1$ if ijk are in descending order and $\varepsilon_{ijk} = 0$ if any of two of ijk are equal). Individual grains in the aggregate respond to the imposed deformation by a combination of a rigid body rotation and simple shear on three independent slip systems $s = 1,2,3$, each of which is assumed to obey a power-law rheology with an activation stress τ_s and a stress exponent n. The deformation rate of each crystal is described by a local velocity gradient tensor:

$$d_{ij}^\nu = G_{ij}^\nu \gamma_\nu - \varepsilon_{ijk}\omega_k^\nu \quad (3)$$

where ω^ν is the rotation rate of the crystallographic axes and γ_ν is the rate of slip on the weakest slip system. The tensor G_{ij}^ν is equivalent to a Schmidt tensor, and is given by [10]:

$$G_{ij}^\nu = 2\sum_{s=1}^{S} \beta^{s\nu} l_i^{s\nu} n_j^{s\nu} \quad (4)$$

where $l_i^{s\nu}$ and $n_j^{s\nu}$ are respectively unit vectors in the slip direction and normal to the slip plane of slip system s, and:

$$\beta^{s\nu} = \frac{\tau_1 I^{s\nu}}{\tau_s I^{1\nu}} \left| \frac{\tau_1 I^{s\nu}}{\tau_s I^{1\nu}} \right|^{n-1} \quad (5)$$

where $I^{s\nu} = l_i^{s\nu} n_j^{s\nu} E_{ij}$ and $s = 1$ is the weakest slip system. The factor $\beta^{s\nu}$ gives the relative activities of the different slip systems as a function of their critical reference shear stresses and of their orientations relative to the macroscopic strain rate tensor. Here and henceforth, the Einstein summation convention is assumed for all indices, except ν and s.

According to von Mises' criterion, three independent slip systems are not sufficient to accommodate an arbitrary imposed strain rate E_{ij}. Accordingly, Ribe and Yu [10] minimize the volume-averaged difference between the local (grain-scale) and macroscopic deformation of the aggregate ('distortion rate'), subject to the constraints of slip system rheology. In general, the local deformation does not match exactly the imposed deformation, and one needs a small amount of 'extra' deformation of the grains to insure global strain compatibility. In the present model, we suppose that this extra deformation is due to secondary deformation mechanisms like grain-boundary sliding [21,22] or dislocation climb [23]. These mechanisms can account for change of shape, but as they involve off-slip plane dislocations,

they do not induce any rotation of the crystallographic axes of the crystals and thus do not affect the LPO [21]. The deformation of a given grain is thus obtained simply by minimizing the (squared) differential strain rate:

$$\langle R\rangle = \sum_{\nu=1}^{N} f_\nu\ (L_{ij}-d^\nu_{ij})(L_{ij}-d^\nu_{ij}) \tag{6}$$

The residual differential strain rate, $\langle R^*\rangle = \langle R\rangle / (L_{ij}L_{ij})$ obtained after minimization, gives the part of the deformation accommodated by climbing and grain-boundary sliding. For an isotropic aggregate of olivine, this deformation accounts for about 13% of the total deformation, with a minimum value of 9% (for simple shear) and a maximum value of 16% (for uniaxial compression). In the calculations presented hereafter, the 'extra' deformation never exceeded 16% of the total deformation.

The minimization yields a set of $4N$ linear algebraic equations for the quantities γ_ν, ω_i^ν, the solutions of which are:

$$\gamma_\nu = \frac{2G^\nu_{ij}L_{ij} - (L_{ii+1}-L_{i+1i})(G^\nu_{ii+1}-G^\nu_{i+1i})}{2G^\nu_{kl}G^\nu_{kl} - (G^\nu_{kl+1}-G^\nu_{k+1l})(G^\nu_{kl+1}-G^\nu_{k+1\,l})} \tag{7}$$

and

$$\omega_i^\nu = \frac{(L_{i+2i+1}-L_{i+1i+2})}{2} - \frac{G^\nu_{i+2i+1}-G^\nu_{i+1i+2})}{2}\gamma_\nu \qquad (i=1,2,3) \tag{8}$$

In these equations, the cyclically ordered subscripts $(i,i+1,i+2)$ take the values (1,2,3), (2,3,1) and (3,1,2). Finally, the change of the orientation g^ν of each grain is given by the evolution equation for the direction cosines a^ν_{ij},

$$\frac{\mathrm{d}a^\nu_{ij}}{\mathrm{d}t} = \varepsilon_{jkl}a^\nu_{il}\omega^\nu_k \tag{9}$$

This system of equations describes the plastic deformation of the aggregate and gives the evolution of the corresponding LPO.

3. Dynamic recrystallization

3.1. Formalism

Dynamic recrystallization is a common process, observed in almost any material after a certain amount of deformation. According to Poirier and Guillopé [24], dynamic recrystallization is a 'deformation-induced reworking of the grain size, shape or orientation, without chemical change'. It is a complex phenomenon associated with changes of microstructures, crystallographic orientations, and rheological properties. The aim of this paper is to propose a simple model of dynamic recrystallization, incorporating the effect of GBM and nucleation as a function of the density of dislocations. We require this model to be in agreement with observations and with the basic physics of dynamic recrystallization, and to be flexible enough to be used to predict the LPO generated by dynamic recrystallization in an arbitrary mantle flow.

In a deforming crystal, dynamic recrystallization is a function of the stored strain energy. On the one hand, a crystal with a high strain energy tends to be invaded by grains with a low energy, by GBM. On the other hand, a grain with a high energy tends to nucleate new strain-free subgrains which will grow by GBM. The LPO of a crystal aggregate subject to dynamic recrystallization thus reflects the balance between nucleation and migration, as illustrated for different minerals by Wenk and coworkers [17,18].

Because the stored strain energy is a function of the dislocation density, one needs to evaluate the density of dislocations in the aggregate as a function of the orientation of the grains. A complete model should treat the evolution of the dislocation density as a function of strain. However, it has been observed that the dislocation density in deforming olivine crystals reaches a steady state at a very small strain (about 1% [25]). At steady state, both theory and experiments indicate that the dislocation density in olivine depends on the stress according to:

$$\rho \propto b^{-2}\left(\frac{\sigma}{\mu}\right)^p, \tag{10}$$

where b is the length of Burgers' vector and μ is the shear modulus. Simple dislocation theory [21] suggests that $p=2$. However, high-temperature creep experiments on olivine single crystals suggest that p varies between 1.6 [25] and 1.4 [26]. We thus henceforth adopt the value $p=1.5$. According to Eq. 10, one expects a correlation between the Schmidt factor of a grain and its density of dislocations, which is indeed observed for olivine crystals [27].

If there were no nucleation, the stored strain energy density E of a crystal would be just the strain energy stored by the dislocations:

$$E = A\rho\mu b^2 \tag{11}$$

with A a dimensionless constant. In that case, soft grains (those with high Schmidt factors) have a larger strain energy and will be consumed by GBM, while hard grains (low Schmidt factors) will grow preferentially. However, in simple-shear experiments [14], it is observed that the texture is dominated by the soft orientations.

In a highly deformed grain, the density of dislocations and the misorientations can be locally very large, which will induce nucleation. Nucleation occurs mainly by sub-grain rotation and grain-boundary bulging and generates strain-free zones in the parent grain. In that case, the bulk strain energy of a crystal is the sum of non-recrystallized zones and strain-free sub-grains with zero strain energy (see Fig. 1):

$$E = \alpha A\rho\mu b^2 \tag{12}$$

with α the non-recrystallized fraction of the grain. The key point is thus to quantify the recrystallized fraction of the grains.

Wenk and Tomé [18], following the classical theory of nucleation by statistical fluctuations, consider that the nucleation rate is an exponential function of the square of the strain energy. However, it is often considered more appropriate to link the nucleation rate to the misorientation of a grain with respect to its neighbors [24]. Because misorientation is proportional to the density of dislocations, the nucleation rate is thus likely to be a function of the density of dislocations. We

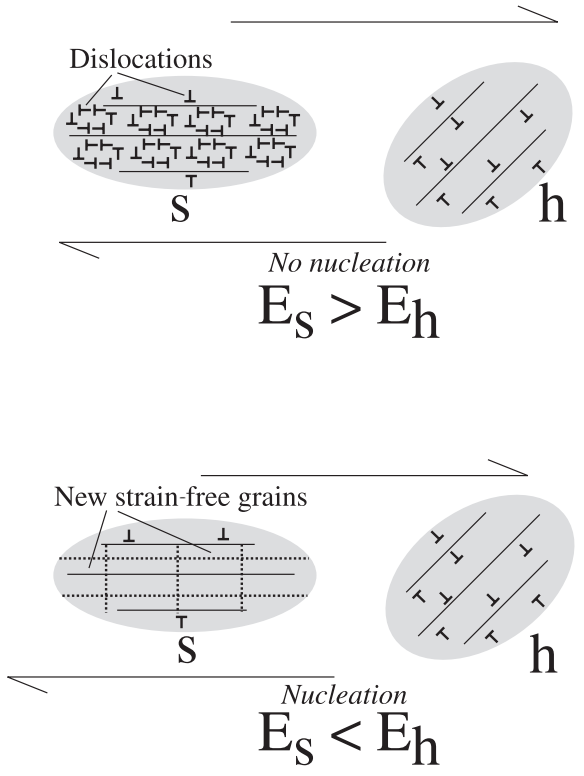

Fig. 1. Dislocation structure and corresponding stored strain energy for a soft grain (s) and a hard grain (h) deformed in simple shear, with and without nucleation. Because nucleation generates strain-free nuclei, the bulk strain energy of the recrystallized soft grain is smaller than that of the hard grain.

assume that the recrystallized fraction of a grain is an exponential function of the square of its misorientation (i.e. of the square of its dislocation density, and thus of the square of its strain energy, as in [18]):

$$\alpha = \exp[-\lambda\ \rho^2] \tag{13}$$

where λ is a 'nucleation parameter', which characterizes the efficiency of nucleation. For large values of λ nucleation is very efficient ($\alpha \to 0$) whereas for small values of λ nucleation is slow ($\alpha \to 1$). This relationship reflects the basic physical link between dislocation density and nucleation, and has the advantage of allowing a simple parametrization of the phenomenon.

Using the strain energy given by Eq. 12, it is

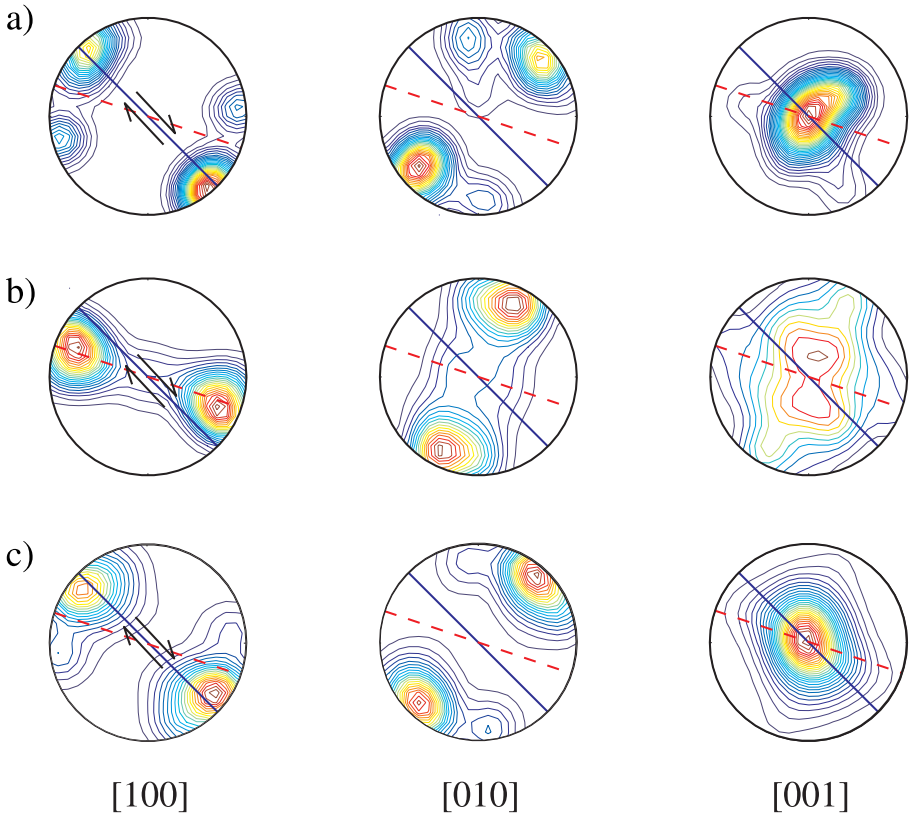

Fig. 2. Pole figures (Lambert equal-area projection, contours at 0.1 m.r.d. (multiples of a random distribution)) for the [100], [010] and [001] crystallographic axes of olivine, in the reference frame defined by the principal axes of the strain rate tensor. The solid line represents the shear plane, and the dashed line the foliation. (a) Experimental results for an olivine aggregate deformed by simple shear at 1573 K (150% finite strain) [14]; (b) prediction of the kinematic constraint theory [10] for an initially isotropic aggregate of 1000 grains deformed by the same amount in simple shear; (c) prediction of the present model for $M^* = 50$ and $\lambda^* = 5$.

straightforward to describe the migration of the grain-boundaries in the aggregate. The migration velocity of a grain-boundary is proportional to the difference of strain energy between grains. Accordingly, we consider that the change of volume of a given grain is proportional to the difference between its strain energy and the average energy $\bar{E}$ of the aggregate. If f is the volume fraction of the grain, the evolution equation has the form:

$$\frac{\mathrm{d}f}{\mathrm{d}t} = -Mf(E-\overline{E}) \qquad (14)$$

where M is the grain-boundary mobility, which characterizes the efficiency of GBM. If a grain has a larger strain energy than the aggregate average energy, it will shrink, whereas it will grow if its energy is lower than the average. We can now incorporate Eqs. 12 and 14, in the model of plastic deformation.

3.2. Kinematic model of dynamic recrystallization

To link recrystallization and plastic deformation we need to relate the density of dislocations in a crystal to its deformation. To do that we first define a reference state for the crystals, such that a reference resolved shear stress τ^s_{ref} on slip system s corresponds to a shear rate $\dot{\varepsilon}_{\mathrm{ref}}$ on the slip plane. Let the associated density of dislocations be ρ^s_{ref}. If we define $s = 1$ as the softest slip system for example, ρ^1_{ref} is the density of dislocations on the slip plane if the applied stress is τ^1_{ref} or equiv-

alently if the strain rate is $\dot{\varepsilon}_{\mathrm{ref}}$. We now express the density of dislocations on a slip plane s for an arbitrary deformation in terms of the reference values.

By Eq. 10, the dislocation density ρ_s on a slip system s is proportional to the power p of the resolved shear stress τ^s acting on that slip plane. Moreover, $\tau^s \propto |\dot{\varepsilon}_s|^{1/n}$, where n is the power-law exponent that characterizes the rheology of the slip systems. Thus:

$$\frac{\rho^s}{\rho^s_{\mathrm{ref}}} = \left(\frac{\tau^s}{\tau^s_{\mathrm{ref}}}\right)^p \equiv \left|\frac{\dot{\varepsilon}^s}{\dot{\varepsilon}_{\mathrm{ref}}}\right|^{p/n} \tag{15}$$

The related stored strain energy is:

$$E_s = A\mu b^2 \rho_s \exp(-\lambda\ \rho_s^2) \tag{16}$$

where the exponent function accounts for the fraction of the strain energy released by nucleation of strain-free sub-grains. We define the total stored strain energy in a grain as the sum of the contributions from the different slip systems:

$$E = A\mu b^2 \sum_s \rho^s_{\mathrm{ref}} \left|\frac{\dot{\varepsilon}^s}{\dot{\varepsilon}_{\mathrm{ref}}}\right|^{p/n} \exp\left[-\lambda \left(\rho^s_{\mathrm{ref}} \left|\frac{\dot{\varepsilon}^s}{\dot{\varepsilon}_{\mathrm{ref}}}\right|^{p/n}\right)^2\right] \tag{17}$$

One may use a more complex definition of the total strain energy, including non-linear terms representing the interactions between dislocations arising from different slip systems during nucleation. However, as no theoretical background is available to describe the phenomenon in detail, we choose the simplest expression for the total strain energy.

To close the system, we need a last relationship between the reference dislocation densities for the different slip systems. These densities are those required to accommodate the strain rate $\dot{\varepsilon}_{ref}$ on the respective slip planes, and are given by Orowan's equation:

$$\dot{\varepsilon}_{\mathrm{ref}} = \rho^s_{\mathrm{ref}} b v^s \tag{18}$$

with v^s the average velocity of the dislocations on the slip plane s. The dislocation density for the slip system s is related to the dislocation density for the softest slip system $s=1$ by:

$$\frac{\rho^s_{\mathrm{ref}}}{\rho^1_{\mathrm{ref}}} = \frac{v^1}{v^s} \tag{19}$$

Because the strain rate is proportional to the stress to the power n and because the dislocation density is proportional to the stress to the power p, Orowan's equation (Eq. 18) indicates that the velocity of dislocations is proportional to the stress to the power $n-p$. In that case we have:

$$\frac{\rho^s_{\mathrm{ref}}}{\rho^1_{\mathrm{ref}}} = \frac{v^1}{v^s} = \left(\frac{\tau^1_{\mathrm{ref}}}{\tau^s_{\mathrm{ref}}}\right)^{n-p} = \left(\frac{1}{\tau^s_0}\right)^{n-p} \tag{20}$$

where $\tau_0{}^s$ is the normalized (dimensionless) reference critical shear stress for the slip system s. By definition, $\tau^1_0 = 1$. If we take $\rho^1_{\mathrm{ref}} = \rho_0$ as the dislocation density scale for the problem, and $\dot{\varepsilon}_{\mathrm{ref}} = \dot{\varepsilon}_0$ as the strain rate scale for the problem, we obtain the expression for the density of mobile dislocations for slip plane s:

$$\rho^s = \rho_0 \left(\frac{1}{\tau^s_0}\right)^{n-p} \left|\frac{\dot{\varepsilon}^s}{\dot{\varepsilon}_0}\right|^{p/n} \tag{21}$$

The total stored energy in the crystal is a function of the total density of dislocations, whereas Orowan's equation gives only the density of mobile dislocations. However, the additional dislocations locked in the cell walls do not drive GBM, as they belong by definition to the two grains separated by the wall. The expression for the stored strain energy driving GBM is thus:

$$E = A\mu b^2\ \rho_0 \sum_s \left(\frac{1}{\tau^s_0}\right)^{n-p} \left|\frac{\dot{\varepsilon}^s}{\dot{\varepsilon}_0}\right|^{p/n} \exp\left\{-\lambda\ \rho_0^2 \left[\left(\frac{1}{\tau^s_0}\right)^{n-p} \left|\frac{\dot{\varepsilon}^s}{\varepsilon_0}\right|^{p/n}\right]^2\right\} \tag{22}$$

Once the energy has been estimated by Eq. 22 (which includes the effect of the nucleation of strain-free grains), the effect of GBM can be calculated using the GBM equation (Eq. 14). Taking $\dot{\varepsilon}_0 = \sqrt{E_{ij}E_{ij}/2}$ as the shear rate scale, we obtain the non-dimensional version of the GBM equa-

tion:

$$\frac{\mathrm{d}f_\nu}{\mathrm{d}t^*} = -M^* f_\nu \left\{ \sum_s \left(I_\nu^{s^*} \exp\left[-\lambda^* (I_\nu^{s^*})^2\right]\right) - \sum_\eta f_\eta \sum_s \left(I_\eta^{s^*} \exp\left[-\lambda^* (I_\eta^{s^*})^2\right]\right)\right\} \quad (23)$$

where $t^* = \dot{\varepsilon}_0 t$ is the dimensionless time and:

$$I_\nu^{s^*} = \left(\frac{1}{\tau_0^s}\right)^{n-p} \left|\frac{\dot{\varepsilon}_\nu^s}{\dot{\varepsilon}_0}\right|^{p/n} \quad (24)$$

are dimensionless Schmidt factors. The sum:

$$I_\nu^* = \sum_s I_\nu^{s^*} \quad (25)$$

defines the average dimensionless Schmidt factor for grain ν, and quantifies the influence of the orientation and of the hardnesses of the slip systems on plastic deformation. Eq. 23 contains in addition two free dimensionless parameters: the nucleation parameter:

$$\lambda^* = \lambda\ \rho_0^2 \quad (26)$$

which characterizes the efficiency of nucleation, and the grain-boundary mobility:

$$M^* = \frac{A\mu b^2 \rho_0 M}{\dot{\varepsilon}_0} \equiv \frac{A\mu b M}{v} \quad (27)$$

which characterizes the efficiency of GBM. The second of the two equivalent expressions for M^* in Eq. 27 is obtained by applying Orowan's Eq. 18.

For given choices of M^* and λ^*, the calculation of the texture evolution requires the following steps for each increment of the imposed deformation:

1. Calculation of ω_k^ν using the minimization Eqs. 7 and 8.
2. Calculation of the new grain orientations using the time evolution Eq. 9.
3. Calculation of the changes of volume fractions due to GBM using the GBM Eq. 27. If the volume fraction of a grain decreases to zero, it is withdrawn from the aggregate.

In the following, we assume that the active slip systems for olivine at high temperature are (010)[100], (001)[100] and (010)[001]. The flow law for these slip systems is inferred from laboratory deformations of olivine single crystals [18–32]. According to the available measurements, the stress exponent is $n \approx 3.5 \pm 0.1$. The softest slip system is (010)[100], and by definition has a normalized reference resolved shear stress $\tau_0^1 = 1$. The hardness of the second slip system (001)[100] depends on the oxygen fugacity, and lies in the range $1 \leq \tau_0^2 \leq 2$. We assign to the hardest slip system (010)[001] a value $\tau_0^3 = 3$ [30]. Using these values of the reference shear stresses, we now calculate the LPO of an aggregate of $N = 3000$ olivine crystals as a function of the imposed deformation and of the model parameters, and compare it with experimental results.

4. Comparison with experiments

To validate the theory, we first compare our predictions with the more complete data set of Zhang and coworkers [14,33] for simple shear. We then show the agreement between the theory and the observations of Nicolas and coworkers [20] in uniaxial compression. The results obtained by Bystricky and coworkers [19] are largely in agreement with the results of Zhang and coworkers [14,33], and we will only address the discrepancy between the two sets of experiments. We first present the model results using the set of parameters that yields the best agreement with the simple-shear observations. We then discuss the influence of the parameters τ_0^2, M^*, and λ^* on the model predictions.

4.1. Simple-shear experiments

4.1.1. Direct comparison

Zhang and Karato [14] performed the first experimental deformation of an olivine aggregate in simple shear. The LPO they obtained is described in detail in [33], using measurements of the orien-

tations of both relict and newly recrystallized grains. The mean orientation of the relict grains follows the strain ellipsoid up to a shear strain of 1, in agreement with the predictions of the classical models of plastic deformation [9,10,12,13]. At larger strains, however, the relict grains are such that their [100] axis is parallel to the shear direction and not to the long axis of the FSE. The LPO of newly recrystallized grains is more complex, as they are either aligned with the shear direction, or perpendicular to the maximum compressional stress [33].

Fig. 2a shows the LPO of an experimental sample deformed to 150% strain ($t^* = 1.06$) at 1573 K [14]. The pole figures represent the orientation distribution of the three crystallographic axes, obtained from the orientation distribution function (ODF). The ODF was generated from measured individual grain orientations by considering each orientation as a Gaussian distribution centered on the measure and with a standard deviation of five degrees. Fig. 2b gives the prediction of the kinematic constraint model of Ribe and Yu [10] without recrystallization for the same finite strain. The LPO follows the FSE and is not aligned with the shear plane. Fig. 2c gives the prediction of the present dynamic recrystallization model with $\tau_0^2 = 2$, $M^* = 50$, and $\lambda^* = 5$. The theory predicts correctly the reorientation of the recrystallized grains on the shear plane, although the pattern of the LPO is somewhat smoother than that observed. The grains with their [100] axis aligned with the shear direction display the largest Schmidt factor I^*. They thus have a large density of dislocations, but because nucleation is active, they nucleate strain-free sub-grains and have a low bulk strain energy. These grains are thus favored by GBM, which generates a peak orientation on the shear plane. A secondary peak observed in the experiments about 45° away from the main peaks is also predicted by the model, but with a smaller intensity. This secondary peak, which is also predicted by plastic models without dynamic recrystallization [12], corresponds to hard grains with low dislocation densities that have not yet been consumed by GBM. It tends to disappear at larger strain, and does so faster for larger grain-boundary mobilities.

So far, we have compared the predicted LPO with that due to porphyroclasts only (Fig. 1). However, the LPO predicted by the model includes by definition both porphyroclasts and recrystallized grains. It is not possible to separate the two populations in the model, because we use a statistical description of nucleation. Nevertheless, in the model the recrystallized grains are predicted to be aligned with the softest orientations, as they are associated with a larger density of dislocations, and thus a larger nucleation rate. Some fraction of the grains newly formed during the experimental deformation is aligned with the shear axis, and our model indicates that this orientation is actually the orientation of maximum nucleation. The second family of recrystallized grains is perpendicular to the maximum compressive stress. The Schmidt factor I^* for this orientation is actually large – because both the (010)[100] and (001)[100] are activated in that orientation –

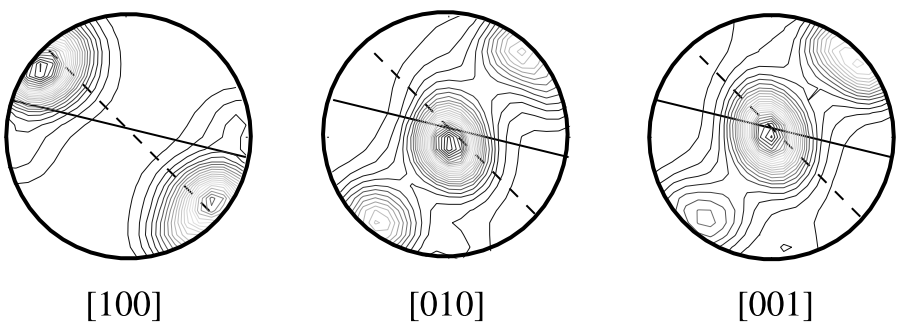

Fig. 3. Same as Fig. 2c, but with slip systems (001)[100] and (001)[100] of equal softness ($\tau_0^1 = \tau_0^2 = 1$). The [010] and [001] axes display a similar pattern, in better agreement with Bystricky and coworkers [19] than with Zhang and Karato [14].

which indicate a favorable orientation for nucleation. The orientations of recrystallized grains in the experiments correspond then logically to the orientations of preferred nucleation in the model

4.1.2. Influence of the model parameters

The model of dynamic recrystallization involves two free parameters, the nucleation parameter λ^* and the grain-boundary mobility M^*, whereas plastic deformation is a function of the reference critical resolved shear stresses τ_0^s. Fortunately, these parameters have very distinct influences on the LPO and can thus be constrained independently by the available data.

The most uncertain of the normalized critical shear stresses is that for the (001)[100] slip system, $1 \leq \tau_0^2 \leq 2$. Fig. 3 shows the pole figures obtained for the same parametrization of recrystallization as before ($M^* = 50$, $\lambda^* = 5$), but for $\tau_0^2 = 1$ instead of $\tau_0^2 = 2$. The [001] and the [010] pole figures are now quite similar, in better agreement with Bystricky and coworkers [19] than with Zhang and Karato [14] (see figure 4 of [19]). The [100] axes lie between the direction of the long axis of the FSE and the shear direction. They rotate towards the shear direction if one increases the grain-boundary mobility. This indicates that dynamic recrystallization is less effective if there are two equally soft slip systems, because plastic deformation is relatively easier in that case. If $\tau_0^2 = 2$, the symmetry is broken, and the [001] pole figure displays a central peak, in better agreement with the experimental data of Zhang and Karato [14]. In the following we therefore use $\tau_0^2 = 2$.

The nucleation parameter λ^* controls the efficiency of nucleation and determines the orientations that will grow by GBM. For values of λ^* smaller than 3, nucleation is not very efficient, and the bulk strain energy of hard orientations is smaller than that of soft orientations. The resulting LPO is such that a large fraction of the [100] axes is normal to the shear direction, in complete disagreement with the experiments. Fig. 4 shows the LPO obtained for $\lambda^* = 2$. A strong peak normal to the shear direction appears in the [100] pole figure. This peak gets stronger for smaller values of the nucleation parameter. The [010] and [001] pole figures are also quite different from the observations. For values larger than 3, nucleation is more efficient, the soft orientations recrystallize preferentially and their bulk strain energy is low. The resulting LPO is such that the [100] axis of the crystals is aligned with the shear direction, in agreement with experiments. The absolute value of λ^* has no significant influence on the LPO development as long as it is larger than 3, because the orientations favored by dynamic recrystallization do not change. For values of λ^* larger than about 50 however, nucleation is so efficient that the stored strain energy becomes negligible in the grains, completely damping GBM. In that case, the LPO will follow the FSE. We take $\lambda^* = 5$ as a reference value because it leads to the best agreement with the experiments of Zhang and Karato [14], and we study in detail the influence of the dimensionless grain-boundary mobility M^*.

The value of M^* (Eq. 27) is a function the in-

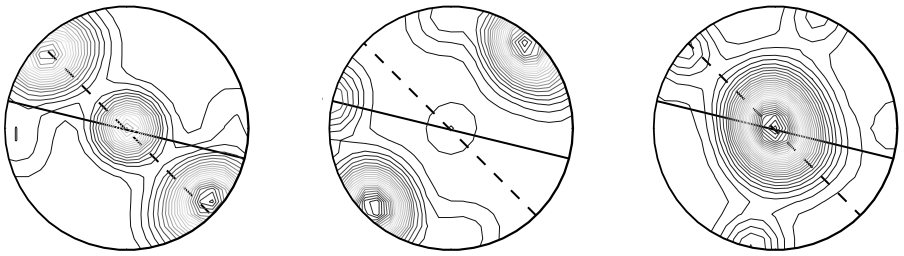

Fig. 4. Same as Fig. 2c, but with less efficient nucleation ($\lambda^* = 2$). Hard orientations are favored by GBM, and a strong additional peak appears in the [100] pole figure, which is not observed in experiments.

trinsic grain-boundary mobility M, the dislocation velocity v, and the unknown constant A. Among these parameters, some constraints are available on the grain-boundary mobility [34], but the proposed values are highly sensitive to the experimental conditions, like the amount of water or the impurity concentration in the boundaries [21]. It is thus difficult to constrain M^* a priori. However, because the experiments of Zhang and Karato [14] give the LPO as a function of strain, they provide strong additional constraints on M^*, which is the main parameter that controls the rate of growth of the peaks of the LPO.

Fig. 5 shows the evolution of the average orientation if the [100] axis relative to the shear direction from [14], and the predictions of our model for three different values of M^*: 0, 50 and 200. If $M^* = 0$, there is no GBM, and the LPO follows the FSE because the deformation is purely plastic [13]. For larger mobilities, the average orientation of the aggregate rotates faster towards the shear plane. Values of M^* between 50 (for the low-temperature experiments) and 200 (for the high-temperature experiments) lead to acceptable predictions. Only three points obtained at high temperature require a substantially larger grain-boundary mobility ($M^* > 300$). One possible explanation is that the grain-boundary mobility increases with temperature, or depends on such additional factors as water content and the concentration of impurities on grain-boundaries which may vary from sample to sample. However, we also note that two of the data in question correspond to very low strain, and are therefore probably not reliable because the weak texture is still influenced by the small initial anisotropy. We therefore believe that $M^* = 200$ is a reasonable value for the high-temperature grain-boundary mobility given the currently available experiments. The range of estimates $M^* = 125 \pm 75$ does not seem unreasonable in view of the likely variability of grain-boundary mobility.

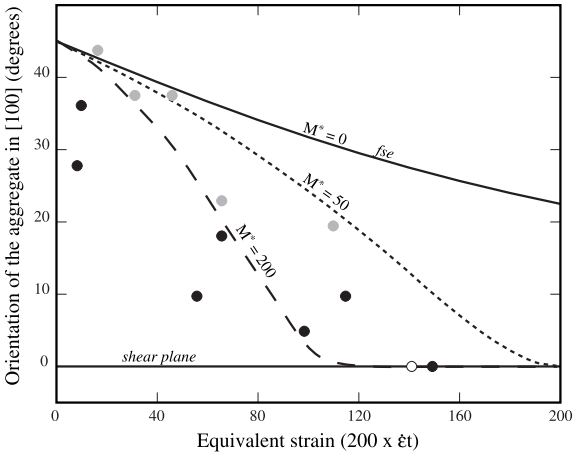

Fig. 5. Evolution of the mean angle between the [100] axes in the aggregate and the shear direction as a function of finite strain in simple shear. The circles represent the experimental results of Zhang and Karato [14] at 1573 K (black), at 1473 K (gray), and under water-saturated conditions (white). The lines give the predictions of the model for various values of dimensionless grain-boundary mobility M^*. For $M^* = 0$, the LPO follows the FSE, whereas it rotates towards the shear plane for increasing M^*.

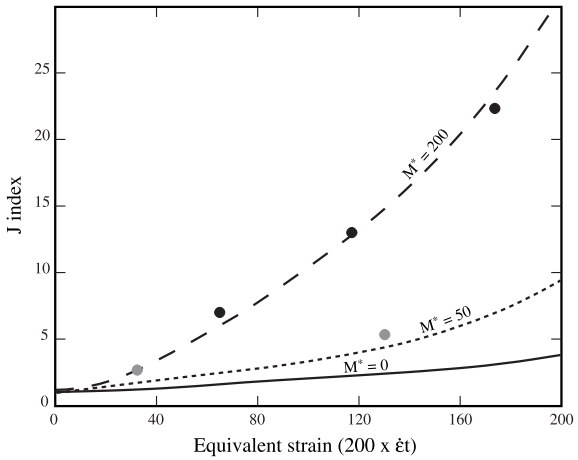

Fig. 6. Evolution of the J-index (Eq. 28) as a function of the finite strain for simple-shear deformation. The circles, which have the same meanings as in Fig. 5, represent the experimental results of Zhang and Karato [14] as estimated by Tommasi and coworkers [12]. The lines give the predictions of the model for various values of M^*. Values of M^* between 50 and 200 lead to predictions in agreement with the experiments.

A second constraint on M^* is obtained from the evolution of the so-called 'J-index' [35]:

$$J = \int f^2(g)\mathrm{d}g \tag{28}$$

which describes the sharpness of the LPO. Fig. 6

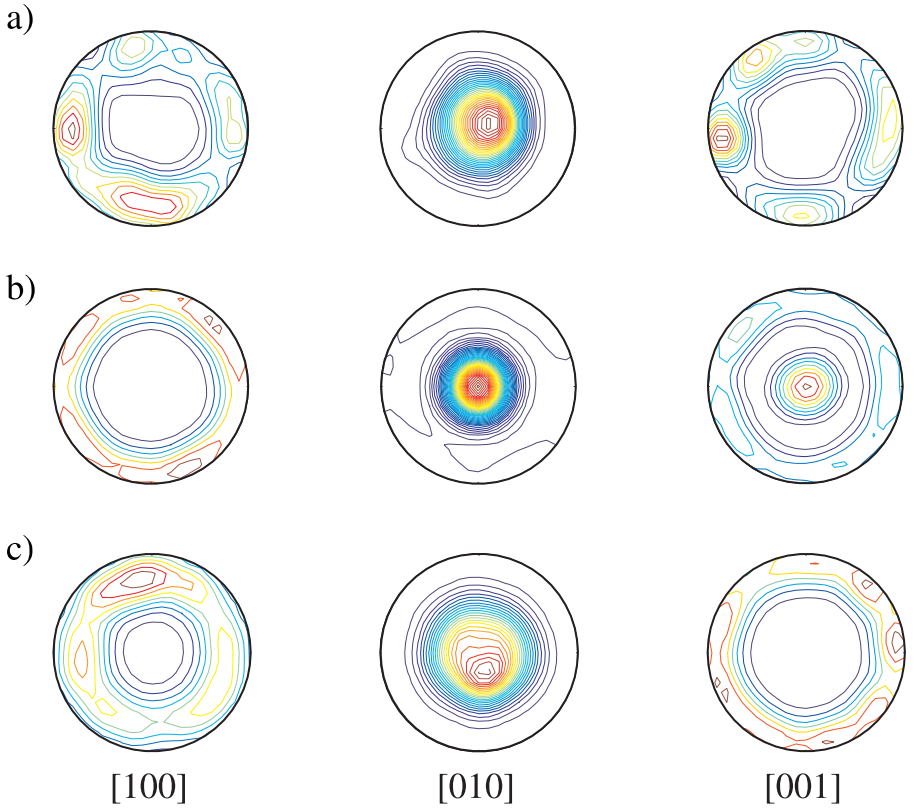

Fig. 7. Pole figures (Lambert equal-area projection, contour interval 0.1 m.r.d.) for the [100], [010] and [001] crystallographic axes of olivine, in the reference frame defined by the principal axes of the strain rate tensor for uniaxial compression (58% shortening). The shortening direction is at the center of each diagram. (a) Experimental results from Nicolas and coworkers [20]; (b) prediction of the kinematic constraint model [10] theory for an initially isotropic aggregate of 1000 grains; (c) prediction of the present model for $M^* = 50$ and $\lambda^* = 5$. The secondary peak in the [001] figure predicted by kinematic plastic models [10], corresponding to a hard orientation, disappears if dynamic recrystallization is active.

shows the comparison between the values of J predicted by our model with those calculated from the experiments of Zhang and Karato [14] by Tommasi and coworkers [12]. Again the results of the model are acceptable for values of M^* between 50 and 200, providing further support for our estimate $M^* = 125 \pm 75$.

4.2. Uniaxial compression

Experiments in uniaxial compression have been performed by Nicolas and coworkers [20]. Fig. 7a shows the pole figures corresponding to the LPO measured for a synthetic dunite shortened by 58% in axial compression [20] ($t^* = 1.06$). This LPO is at first order in agreement with the LPO predicted by purely plastic deformation models [9,10], as shown in Fig. 7b. However, the purely plastic deformation model predicts a strong peak of [001] axes parallel to the direction of shortening, corresponding to a hard orientation, which is not observed in the experiments. Fig. 7c shows the predictions of the dynamic recrystallization model using the same parameters as for the simple-shear case ($\tau_0^2 = 2$, $\lambda^* = 5$ and $M^* = 50$), and for the same finite strain as in the experiment. The additional peak vanishes when dynamic recrystallization is active. The overall agreement between the experiment and the model predictions is good, although the predicted LPO is noticeably weaker than the experimental LPO. A better agreement could be obtained by using a larger grain-boundary mobil-

ity, which would sharpen the predicted LPO. Another possible explanation of the discrepancy is that the experimental pole figures do not include the more random component of LPO associated with small recrystallized grains [12].

5. Discussion

The principal goal of our work has been to develop a model of dynamic recrystallization that is both realistic enough to match experimental data and simple enough for application to the complex deformation histories occuring in the Earth's mantle. The plastic flow portion of the model is analytical, which makes the numerical code both efficient and stable. Obviously, a numerical algorithm for calculating LPO can only be included in mantle convection codes if it does not overwhelm the calculation of the convective flow itself. The present semi-analytical model is more than two orders of magnitude faster than the matrix-based kinematic constraint model of Ribe and Yu [10], which is in turn about two orders of magnitude faster than a VPSC code [10], yielding a savings in computer time of some four orders of magnitude. Numerical codes for equilibrium-based models (EQBA) are faster than VPSC ones, but our code is still at least one order of magnitude faster than EQBA (for the same time stepping scheme; A. Tommasi, personal communication, 2001). The present model is therefore practical for use in the direct calculation of anisotropy in convective flows.

In our theory, dynamic recrystallization depends on only two free parameters that can be constrained by available laboratory experiments: the nucleation parameter λ^* and the dimensionless grain-boundary mobility M^*. We have seen that a nucleation parameter $\lambda^* > 3$ leads to predictions in good agreement with experimental observations. If nucleations were less efficient in the mantle, one would expect hard orientations to dominate the LPO, which is contrary to observations of natural samples of mantle peridotites [36]. A value $\lambda^* = 5$ is probably suitable for the mantle, as the exact value of λ^* (between 3 and 50) does not significantly influence the LPO.

Our results further show that a dimensionless grain-boundary mobility $M^* = 125 \pm 75$ is in agreement with the LPO evolution at low and at high temperatures. If temperature is the main controlling factor of GBM in the mantle, these values are probably suitable for the Earth too. However, the laboratory experiments are performed at stresses much higher than those in the upper mantle. If the absolute value of the stress controls dynamic recrystallization, there is no way to extrapolate the experimental results to the mantle. That is a problem faced by all rheological models. However, it is important to note that our dimensionless grain-boundary mobility M^* depends only on the ratio M/v of the intrinsic grain-boundary mobility and dislocation velocity. Thus M^* will be relatively constant if both M and v depend in the same way on stress, a reasonable first-order assumption.

A last unknown is the activity of the (001)[100] slip system relative to the (010)[100] slip system. We have seen that this depends on the oxygen fugacity which can vary from place to place in the mantle. However, the value of τ_0^2 mainly affects the [001] (c) axes orientation, whereas the [100] (a) axes always rotate towards the shear direction. For seismic anisotropy, the orientation of the axis of fastest seismic wave propagation, the (a) axis, is the most relevant, and the exact value of τ_0^2 is of little importance. Additionally, recent experiments [37] indicate that water content in olivine may have a large influence on the relative strengths of the slip systems, and can induce different LPO from that obtained under water-poor conditions. This effect can easily be incorporated in the model when the experimental data become sufficient to constrain it. For now however, because the large majority of natural samples display an LPO in agreement with experimentally obtained LPO [12], we consider that $\tau_0^1 = 1$, $\tau_0^2 = 2$, and $\tau_0^3 = 3$ are reasonable choices for the conditions in the mantle.

In conclusion, given the good agreement between the model predictions and the laboratory experiments, and given the uncertainties involved in the definition of the model parameters, we propose that the present theory can be used to investigate the relationship between seismic anisotropy

in the mantle and the convective flow which causes it. A suitable set of model parameters is $\tau_0^2 = 2$, $\lambda^* = 5$ and $M^* = 125$. The application of the model to the Earth will be the object of a companion paper.

Acknowledgements

We are grateful to S.-I. Karato, J.-P. Poirier, A. Tommasi, and J. Tullis for fruitful discussions during the maturation of the manuscript. S.-I. Karato and S. Zhang generously made available to us the experimental data from [14]. We also thank Marc Zimmerman and an anonymous reviewer for their comments.*[AC]*

References

[1] J.P. Montagner, Can seismology tell us anything about convection in the mantle?, Rev. Geophys. 32 (1994) 115–138.
[2] D.W. Forsyth, The early structural evolution and anisotropy of the oceanic upper mantle, Geophys. J. R. Astron. Soc. 43 (1975) 103–162.
[3] L.P. Vinnik, G.L. Kosarev, L.I. Makeyeva, Anisotropy of the lithosphere from observations of waves SKS and SKKS, Dokl. Akad. Nauk. USSR 278 (1984) 1335–1339.
[4] H. Hess, Seismic anisotropy of the uppermost mantle under the oceans, Nature 203 (1964) 629–631.
[5] D. Anderson, Theory of the Earth, Blackwell Scientific Publications, Oxford, 1989.
[6] A. Nicolas, N.I. Christense, Formation of anisotropy in upper mantle peridotites: A review, in: K. Fuchs, C. Froidevaux (Eds.), Composition, Structure and Dynamics of the Lithosphere-Asthenosphere System, Geodyn. Monogr. Ser., AGU, Washington, DC, 1987, pp. 111–123.
[7] M. Kumazawa, O.L. Andersen, Elastic moduli, pressure derivatives, and temperature derivatives of single-crystal olivine and single-crystal forsterite, J. Geophys. Res. 74 (1969) 745961–745972.
[8] J.P. Montagner, Where can seismic anisotropy be detected in the earth's mantle? In boundary layers, Pure Appl. Geophys. 151 (1998) 223–256.
[9] H.R. Wenk, K. Bennett, G. Canova, A. Molinari, Modelling plastic deformation of peridotite with the self-consistent theory, J. Geophys. Res. 96 (1991) 8337–8349.
[10] N.M. Ribe, Y. Yu, A theory for plastic deformation and textural evolution of olivine polycrystals, J. Geophys. Res. 96 (1991) 8325–8335.
[11] Y.B. Chastel, P.R. Dawson, H.R. Wenk, K. Bennett, Anisotropic convection with implications for the upper mantle, J. Geophys. Res. 98 (1993) 17757–17771.
[12] A. Tomassi, D. Mainprice, G. Canova, Y. Chastel, Viscoplastic self-consistent and equilibrium-based modelling of olivine lattice preferred orientations. 1. Implications for the upper mantle seismic anisotropy, J. Geophys. Res. 105 (2000) 7893–7908.
[13] N.M. Ribe, On the relation between seismic anisotropy and finite strain, J. Geophys. Res. 97 (1992) 8737–8747.
[14] S. Zhang, S.I. Karato, Lattice preferred orientation of olivine aggregates deformed in simple shear, Nature 375 (1995) 774–777.
[15] A. Etchecopar, A plane kinematic model of progressive deformation in a polycrystalline aggregate, Tectonophysics 39 (1977) 121–139.
[16] M.W. Jessell, Simulation of fabric development in recrystallizing aggregates. I. Description of the model, J. Struct. Geol. 10 (1988) 771–778.
[17] H.R. Wenk, G. Canova, Y. Brechet, L. Flandin, A deformation based model for recrystallization, Acta Mater. 45 (1997) 3283–3296.
[18] H.R. Wenk, C.N. Tomé, Modeling dynamic recrystallization of olivine aggregates deformed in simple shear, J. Geophys. Res. 104 (1999) 25513–25527.
[19] M. Bystricky, K. Kunze, L. Burlini, J.-P. Burg, High shear strain of olivine aggregates: rheological and seismic consequences, Science 290 (2000) 1564–1567.
[20] A. Nicolas, F. Boudier, A.M. Boullier, Mechanisms of flow in naturally and experimentally deformed peridotites, Am. J. Sci. 273 (1973) 853–876.
[21] J.-P. Poirier, Creep of Crystals, Cambridge University Press, Cambridge, 1985.
[22] G.E. Jaroslow, G. Hirth, H.J.B. Dick, Abyssal peridotite mylonites: Implications for grain-size sensitive flow and strain localization in the oceanic lithosphere, Tectonophysics 256 (1996) 17–37.
[23] G.W. Groves, A. Kelly, Change of shape due to dislocation climb, Phil. Mag. 18 (1968) 977–986.
[24] J.-P. Poirier, M. Guillopé, Deformation induced recrystallization of minerals, Bull. Mineral. 102 (1979) 67–74.
[25] W.B. Durham, C. Goetze, B. Blake, Plastic flow of oriented single crystals of olivine. 2. Observations and interpretations of the dislocation struction, J. Geophys. Res. 82 (1977) 5755–5770.
[26] Q. Bai, D.L. Kohlstedt, High-temperature creep of olivine single crystals. 2. Dislocation structures, Tectonophysics 206 (1992) 1–29.
[27] S.I. Karato, K.H. Lee, Stress-strain distribution in deformed olivine aggregates: inference from microstructural observations and implications for texture development, Proc. ICOTOM 12 (1999) 1546–1555.
[28] D.L. Kholstedt, C. Goetze, Low-stress high-temperature creep in olivine single crystals, J. Geophys. Res. 79 (1974) 2045–2051.
[29] W.B. Durham, C. Goetze, Plastic flow of oriented single crystals of olivine. 1. Mechanical data, J. Geophys. Res. 82 (1977) 5737–5753.

[30] Q. Bai, S.J. Mackwell, D.L. Kohlstedt, High-temperature creep of olivine single crystals. 1. Mechanical results for buffered samples, J. Geophys. Res. 96 (1991) 2441–2463.
[31] D.R. Hanson, H.A. Spetzler, Transient creep in natural and synthetic, iron-bearing olivine single crystals: Mechanical results and dislocation microstructure, Tectonophysics 235 (1994) 293–315.
[32] Z.M. Jin, Q. Bai, D.L. Kholdstedt, High temperature creep of olivine crystals from four localities, Phys. Earth Planet. Inter. 82 (1994) 55–64.
[33] S. Zhang, S.-I. Karato, J.F. Gerald, U.H. Faul, Y. Zhou, Simple shear deformation of olivine aggregates, Tectonophysics 316 (2000) 133–152.
[34] S.-I. Karato, Seismic anisotropy due to lattice preferred orientation of minerals: kinematic or dynamic, in: M.H. Manghani and Y. Syono (Eds.), High-Pressure Research in Mineral Physics, AGU, Washington, DC, 1987, pp. 455–471.
[35] H.J. Bunge, Texture Analysis in Materials Sciences, Butterworths, London, 1982.
[36] W. Ben Ismail, D. Mainprice, An olivine fabric database: an overview of upper mantle fabrics and seismic anisotropy, Tectonophysics 296 (1998) 145–158.
[37] H. Jung, S.I. Karato, Effects of water on the deformation microstructures in olivine, EOS Trans. Am. Geophys. Un. 48 (Suppl. 81) (2000) 1209.